

EVALUATION OF MORPHOUS WING CHARACTERISTICS IN WATER AND WIND TUNNEL IN THE CONTEXT OF UAV OPERATIONAL FLEXIBILITY

Marta Marciniuk[1], Marek Szumski[2], Zygmunt Szczerba[2], Łukasz Kiszkowiak[3], Łukasz Malicki[1], Paweł Piskur[4], Krzysztof Sibilski[5] & Stanisław Kachel[3]

[1]Faculty of Mechanical and Power Engineering, Department of Cryogenics and Aerospace Engineering, Wrocław University of Science and Technology, 27 Wybrzeże Stanisława Wyspiańskiego Str., 50-370 Wrocław, Poland
[2]Department of Aerospace Engineering, Faculty of Mechanical Engineering and Aeronautics, Rzeszow University of Technology, Al. Powstańców Warszawy 12, 35-959 Rzeszów, Poland
[3]Military University of Technology, Faculty of Mechatronics, Armament and Aerospace, gen. Sylwestra Kaliskiego 2, 00-908, Warsaw, Poland
[4]Polish Naval Academy of the Heroes of Westerplatte, Faculty of Mechanical and Electrical Engineering, Śmidowicza Street 69, 81-127 Gdynia, Poland
[5]Air Force Institute of Technology, Księcia Bolesława 6 Str., 01-494 Warszawa

Abstract

These work evaluates a novel micro-UAV design that utilizes an innovative continuous trailing-edge camber-morphing airfoil, in comparison with the conventional NACA 24012 airfoil. The results show that camber morphing increases lift and delays stall throughout the tested angle of attack (AOA) range, which also introduces the rise in drag. Pitching-moment trends indicate that the baseline airfoil remains statically stable across the useful range of AOA, whereas the cambered configuration maintains static stability up to approximately 20° of AOA. Overall, the implementation of a continuous trailing-edge morphing airfoil to a micro-UAV provides enhanced lift and controllable drag, offering enhancement in landing distance reduction and mitigating damage risk during operations from unprepared terrain.

Keywords: morphing wing, UAV, experimental aerodynamics, mission flexibility

1. Introduction

Morphing wings are widely studied adaptive structures designed to change their shape and adapt to a wide range of flight conditions [1]. Their application is commonly associated with aerodynamic efficiency improvement, as a continuous surface enables a smooth transition between the leading and trailing edges when slightly deflected, which may reduce drag and improve performance [2, 3, 4]. Nevertheless, morphing concepts can also be employed intentionally for drag production when larger deflections are applied. Such an approach is particularly advantageous during approach and landing, as increased drag may reduce airspeed and reduce the required landing distance [5, 6]. Moreover, slight deflections may decrease the influence of wind gusts and support autopilot performance in demanding operating conditions, thereby increasing the operational flexibility of UAVs during missions conducted in hazardous terrain [7].

Nowadays, UAVs are widely utilized for different types of missions in vast and inaccessible or dangerous areas and hazardous terrain [8, 9]. Their applications range from military tasks (defence and surveillance) to civil operations such as linear infrastructure inspection, agricultural crop monitoring, traffic management, and aerial imaging [10, 11, 12]. In many of these scenarios, the lack of a paved runway increases the probability of airframe damage during landing and, at the same time, limits the overall mission flexibility of the UAV due to restricted recovery options and operational constraints in

unprepared terrain [5, 13, 14]. Therefore, solutions enabling controllable drag augmentation are of particular interest, as they may decrease landing distance and reduce damage risk when operating on rough and unprepared landing sites [5, 7, 15].
The aim of this work was to compare the NACA 24012 airfoil with its morphous version with continuous trailing edge morphing, selected from preliminary studies Figure 1 [5, 7, 15]. The tests were carried out on two experimental stands. First, wing cross-section models were examined using the Particle Image Velocimetry (PIV) method in a water tunnel at a Reynolds number of 21,900. Next, a simple geometry of an unmanned aerial vehicle with a flying wing and retractable wings was tested in a wind tunnel, obtaining aerodynamic coefficients at Reynolds numbers of 350,000 and 438,000.

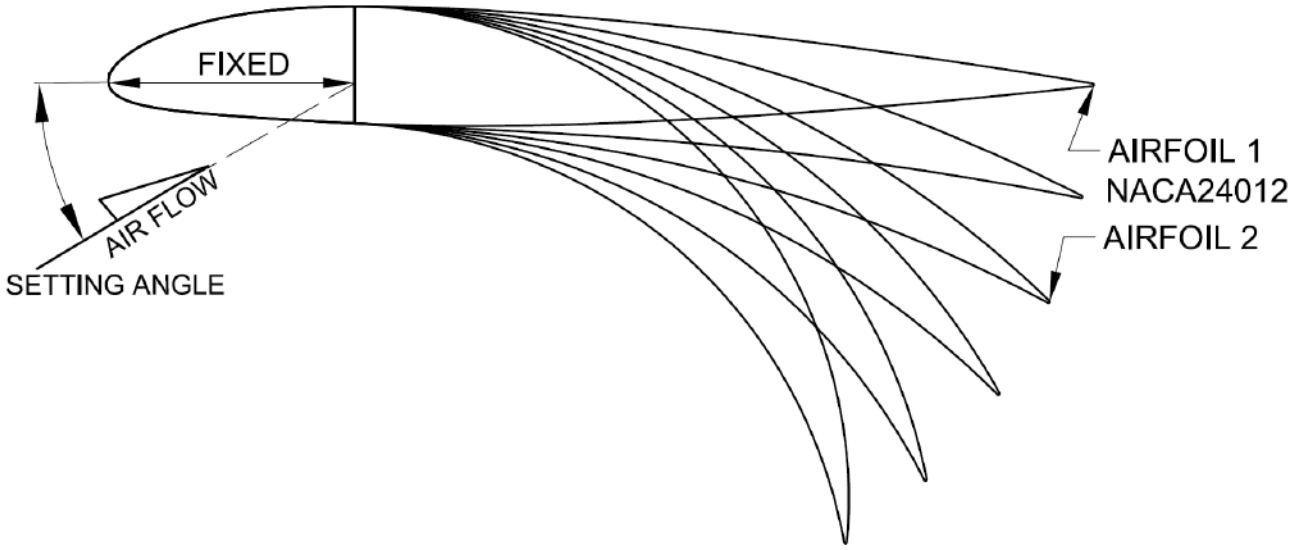


Figure 1 – Camber morphing airfoil geometries. Representation of Airfoil 1 plain NACA24012 airfoil geometry and Airfoil 2 camber morphing airfoil.

2. Materials and Methods

2.1 Models preparation

For the 2D PIV experiments the 3D morphous wings models were created. The wing models were manufactured using 3D printing technology using PLA material. The characteristic for additive printing methods roughness was removed by primer painting and grinding repeated until the smooth surface was achieved. Flowingly, the models were painted in black matt color. For the wind tunnel experiments the UAV model in flying wing configuration was created. The main parameters of the aircraft are presented in Table 1. The model consisted of fuselage with dedicated mounting for aerodynamic balance and retractable wings, which had similar airfoil as models for the PIV experiments. The model was 3D printed and the surface was prepared similarly to previous wing models (Figure 2).

Table 1 – The main parameters of UAV geometry.

Parameter	Value
UAV type	Flying wing
Sweep angle	20°
Wing span	$0.800\,\mathrm{m}$
Wing chord (wing tip)	$0.200\,\mathrm{m}$
Wing chord (fuselage)	$0.275\,\mathrm{m}$
Lift area	$0.2134\,\mathrm{m}^2$



(a)

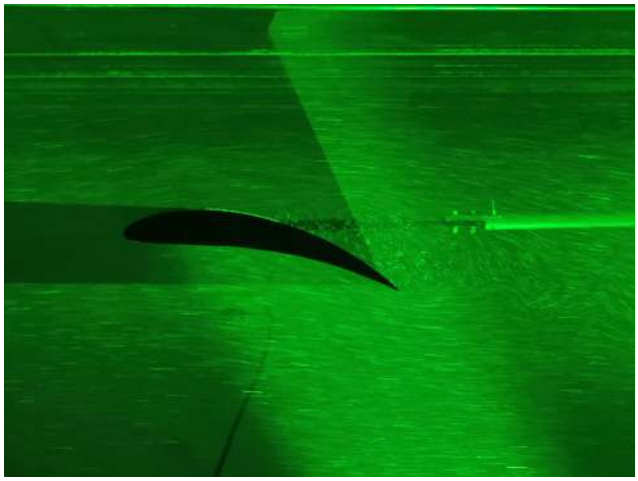


(b)

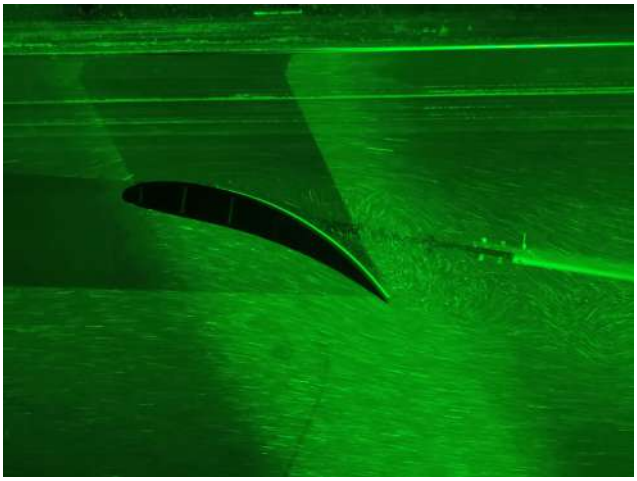
Figure 2 – UAV model preparation: (a) primer painting, (b) black matt color painting

2.2 Water Tunnel

The two-dimensional experiments using the Particle Image Velocimetry (PIV) (Figure 3) method were conducted at the Military University of Technology in the Rolling Hills Research Corporation water tunnel (model 2436). The facility is a closed-circuit tunnel with a rectangular test section of 610 mm × 915 mm. The tunnel is equipped with a three-axis mounting bracket ensuring precise positioning of the test model, as well as instrumentation in the test chamber, including a water-flow velocity meter and a thermometer. The measured velocity and temperature were used to determine the Reynolds number for the operating conditions during the experiments. The attainable free-stream velocity range in the water tunnel is 0–280 mm/s [16, 17, 18].



(a) Airfoil 2 at $\alpha = 0^\circ$



(b) Airfoil 2 at $\alpha = 10^\circ$

Figure 3 – Airfoil 1 and 2 during experiments with visible turbulence in the wake structure.

Particle Image Velocimetry is a non-invasive, image-based method used to determine the velocity field in a selected region of the flow. The PIV procedure follows a standard sequence including image acquisition, pre-processing, image evaluation, post-processing, and data exploration [19, 20]. The measurement accuracy is affected by tracer properties and the experimental arrangement; therefore, the particles should be sufficiently small and close to neutrally buoyant while providing adequate light scattering. The seeding density was adjusted to ensure approximately ten particles within the interrogation window, and the measurement plane was aligned with the main flow direction.
In the water tunnel experiments (Figure 4), silver-coated glass microspheres with a diameter of 10 μm were used as tracers. The flow was illuminated using a pair of 10 W green line lasers and recorded by

a high-speed camera with a resolution of 1024 × 1024 at 1000 frames per second. The flow velocity was in lower range of the water tunnel capabilities and was set to obtain the Reynolds number about 20 000. This range of the flow was intended to represent the flight conditions of the UAV in the last phase of landing approach. The aim was to investigate the flow around the airfoil and determine the flow behavior under very low-speed conditions, with dominant viscous effects. The flow parameters are presented in the Table 2.

Table 2 – The flow parameters in water tunnel during experiments.

Parameter	**Value**
Flow velocity, v	$0.0762\,\mathrm{m/s}$ $(3\,\mathrm{in/s})$
Water temperature, t	$26.3\,^{\circ}\mathrm{C}$
Kinematic viscosity, ν	$8.71 \times 10^{-7}\,\mathrm{m^2/s}$
Reynolds number, Re	$21\,900$

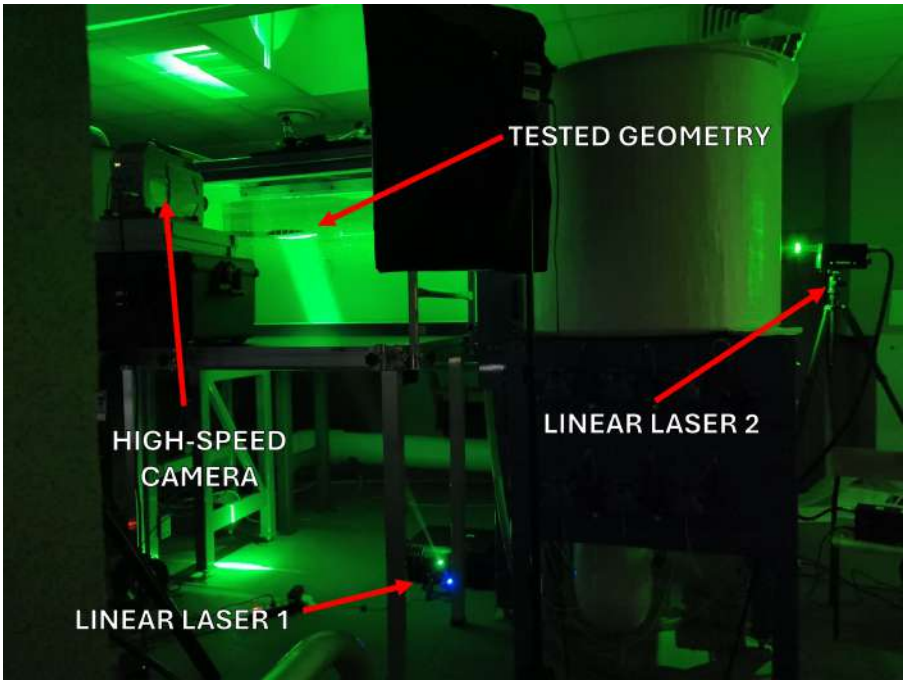
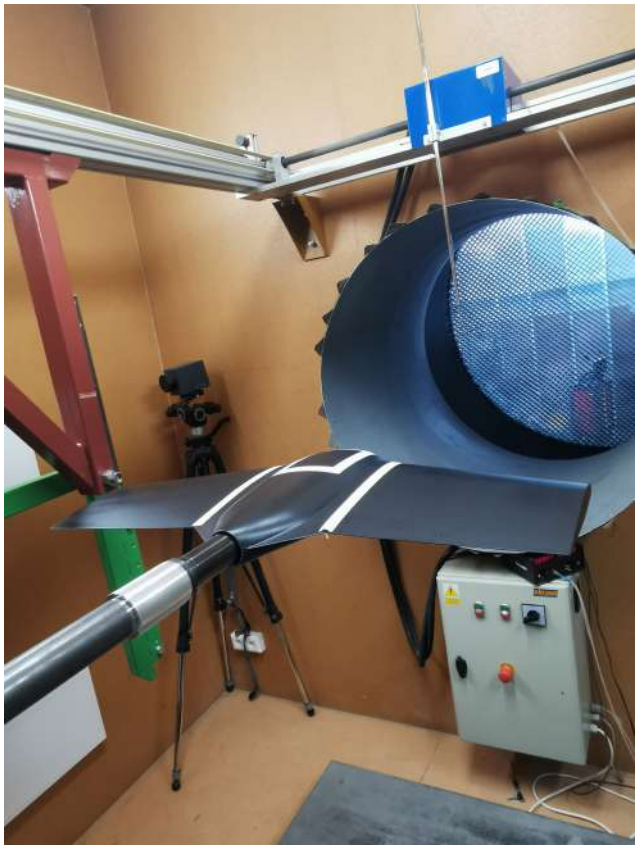


Figure 4 – Water tunnel experimental setup.

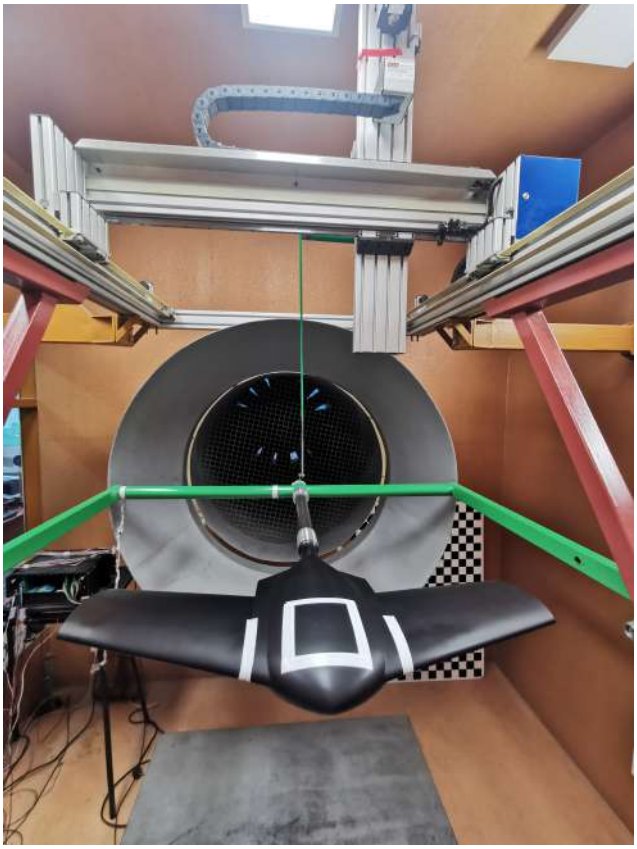
2.3 Wind Tunnel

The tests with UAV geometry were conducted in the TA 1000 wind tunnel at Rzeszow University of Technology. An open-circuit facility was used, equipped with an Eiffel-type measuring chamber of 3 m × 3 m × 3 m and an open test section with a diameter of 1 m and a length of 1.7 m. The maximum free-stream velocity of the tunnel is 55 m/s.

The experimental setup (Figure 5) employed a six-component strain-gauge aerodynamic balance and a sting positioning system enabling precise adjustment of the model angle of attack (AOA). The measurement station was supplemented by dynamic pressure measurements and atmospheric parameter monitoring (pressure, temperature, and humidity). The acquisition system consisted of an IOTech DaqBook 2001 A/D converter with DBK80 (pressure, temperature, and humidity) and DBK16 (forces and moments) expansion cards. During the tests, the model was mounted on the aerodynamic balance and levelled using an inclinometer.



(a) UAV model with Airfoil 1 wing.



(b) UAV model with Airfoil 2 wing.

Figure 5 – Test section of TA1000 wind tunnel in Eiffel-type measuring chamber with mounted UAV model

Measurements were conducted at free-stream velocities of 20 m/s and 25 m/s within the AOA range from $\alpha = -10^\circ$ to 20° in 1° increments. The flow parameters in the wind tunnel are presented in the Table 3. For each measurement point, datasets containing 32,768 samples of instantaneous signals and corresponding averaged values of forces, moments, and dynamic pressure were recorded.

Table 3 – The flow parameters in the wind tunnel during experiments.

Parameter	**Value**
Velocity	20–$25\,\mathrm{m/s}$
Temperature	$22.7\,^\circ\mathrm{C}$
Kinematic viscosity	$1.571 \times 10^{-5}\,\mathrm{m^2/s}$
Pressure	$1027\,\mathrm{hPa}$
Density	$1.19\,\mathrm{kg/m^3}$
Reynolds number for Airfoil 1 at $20\,\mathrm{m/s}$	350,000
Reynolds number for Airfoil 1 at $25\,\mathrm{m/s}$	438,000

2.4 Uncertainties

Due to the complexity of the experiment, the measurement uncertainty has a multi-stage character. A combined Type A/Type B approach was applied. In all cases, the measurement system recorded large series of samples. The formulas presented include terms accounting for both the calibration uncertainty of the measurement chains and the standard uncertainty.

All reported results represent estimated mean values calculated from series of 32,768 samples. The expanded uncertainty was determined using a coverage factor of k = 2, indicating that the true value of the measure lies within the stated interval with a confidence level of approximately 95%.

For the force measurements, the system's static uncertainties were first determined by propagating them from the reference standard through the entire measurement chain. The limit uncertainty of the reference standard under the static conditions of the measurement setup was $\Delta P_{\mathrm{gr}} = 0.1N$. The standard error, determined from the noise recorded during calibration, was $S_P = 0.01N$.
Here, system noise refers to the force values indicated by the measurement system when the tunnel airspeed was zero and the tared balance was not subjected to any aerodynamic loads. Finally, the overall uncertainty of the force determination was calculated using Eq. (1):

$$u(P) = \sqrt{\frac{\left(\Delta P_{\mathrm{gr}}\right)^2}{3} + S_P^2}. \tag{1}$$

The uncertainty of the dynamic pressure measurement was determined analogously, assuming a reference standard limit uncertainty of $\Delta p_{d,\mathrm{gr}} = 1Pa$. The lift and drag coefficients for each tested angle of attack were calculated using the following relation:

$$C_{L,D} = \frac{P_{L,D}}{S p_d}, \tag{2}$$

where C_L is the lift coefficient, C_D is the drag coefficient, P_L is the measured lift force, P_D is the measured drag force, S is the wing reference area, and p_d is the measured dynamic pressure.
Finally, the uncertainty resulting from the accuracy of the measurement chain and the overall combined uncertainty of the lift and drag coefficient measurements were determined using the following formulas:

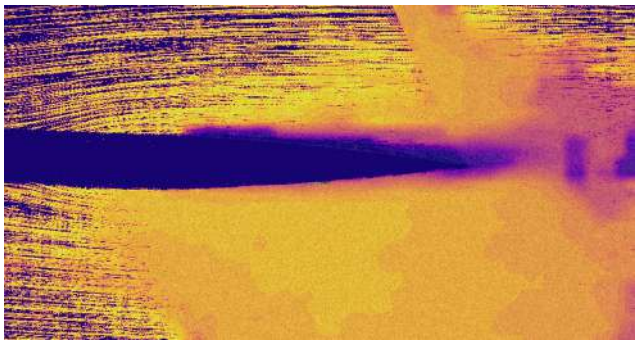
$$u\left(C_{L,D}\right) = \left|\frac{1}{S p_d}\right| \Delta P_{\mathrm{gr}} + \left|-\frac{P_{L,D}}{S p_d^2}\right| \Delta p_{d,\mathrm{gr}} \tag{3}$$

$$u_c\left(C_{L,D}\right) = \sqrt{\left[u\left(C_{L,D}\right)\right]^2 + S_{C_{L,D}}^2}. \tag{4}$$

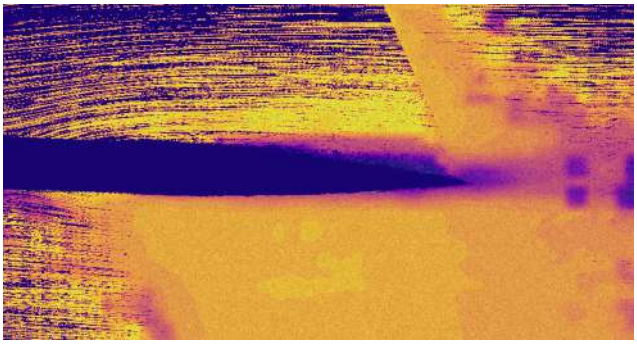
Finally, the error bars were applied to the aerodynamic characteristics charts.

3. Results

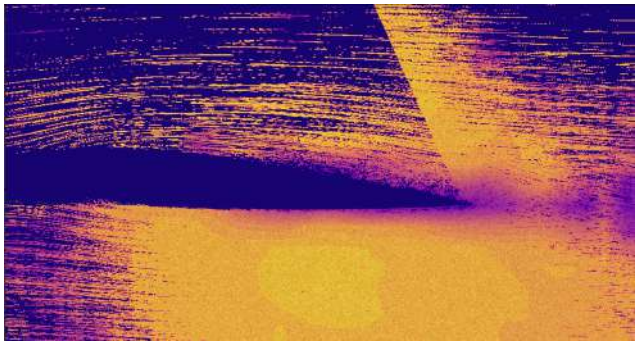
Results obtained from the water tunnel PIV measurements (Figure 6, 7) indicate that increasing the camber deflection substantially modifies the flow around the morphing wing.
Airfoil 1 at $\alpha = 0^\circ$ has organized flow and relatively narrow wake structure. At 2° and 4° the flow separates from upper airfoil surface. The separation point moves from trailing edge to the nose of the airfoil with the increase of the setting angle. For 6° the wake structure becomes broader with the increased field of reduced speed. The setting angles 8° and 10° demonstrate separation with large eddy generation on upper airfoil surface, however the flow in not yet fully separated. The flow separation occurs before half of the airfoil. Above all the tested geometries high-velocity region is formed, which becomes more concentrated with faster airflow accelerating with the increasing setting angle. At high setting angles nearby the trailing edge forms eddy with reversed flow, and at 10° there is visible area of turbulence downstream.
With the increase of the camber the flow becomes chaotic and turbulent even at low setting angles. For Airfoil 2 0° and 2° setting angle the separation point is in about 25% of the chord, and the flow behind the airfoil is turbulent with multiple eddies. The wake structure is however tilted downwards what is the result of camber deflection. Above the airfoil creates high-speed suction region of higher velocity, than for non-deflected airfoil. At 4° the viscosity forces generate the eddy structure behind the airfoil, what causes the high-velocity flow crack in the wake structure. Similar behavior of the flow is observed for 6°. The flow is fully separated and the wake structure is broad and demonstrates high turbulence with local increases in velocity. As for the 8° and 10° the flow is fully separated. The wake structure is more compact, than for 4° and 6° as also its center line is transitioned downwards. The local increases in velocity are no longer observable near the upper surface of the airfoil. Above the geometries the high-velocity suction region is stronger with increased velocity.



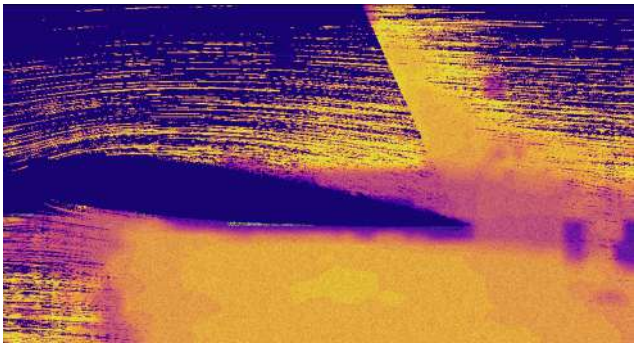
(a) Airfoil 1 $\alpha = 0^\circ$



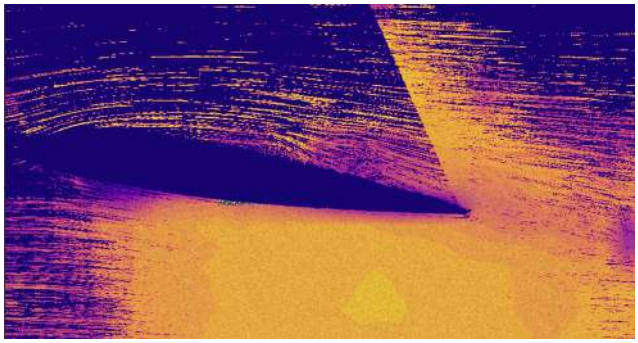
(b) Airfoil 1 $\alpha = 2^\circ$



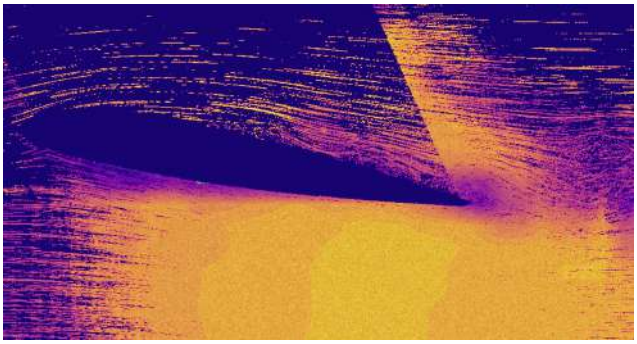
(c) Airfoil 1 $\alpha = 4^\circ$



(d) Airfoil 1 $\alpha = 6^\circ$



(e) Airfoil 1 $\alpha = 8^\circ$

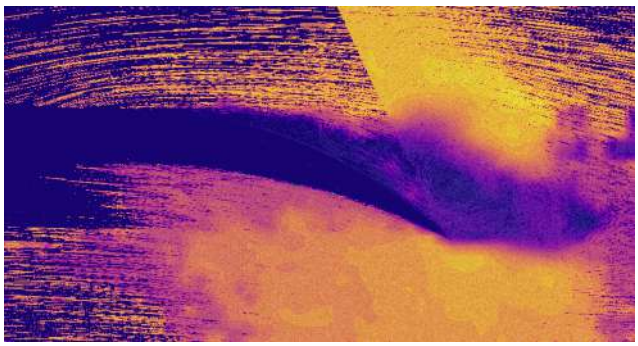


(f) Airfoil 1 $\alpha = 10^\circ$

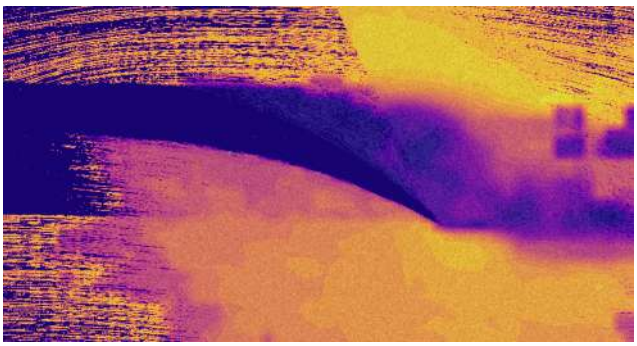
Figure 6 – PIV results with visible streamlines and velocity field distribution around the Airfoil 1.

Summarizing, for non-deflected airfoil, the separation point is shifting towards the leading edge with the increase of the setting angle. However, a complete flow detachment was not observed, while the wake region behind the model increases. With the increasing camber and setting angle the flow becomes dominated by separated shear layer. The wake structure is created from constantly separating and connecting flow, which causes the reversed flow turbulence and local high-velocity regions in the wake structure. Distinct vortical structures develop above the upper surface, which is accompanied by locally increased velocities and a noticeable enlargement of the wake structure. The growth of the wake area suggests an increase in aerodynamic drag and indicates the potential for rapid airspeed reduction when required. At the same time, the intensified vortical structures and higher velocities near the upper surface suggest lift augmentation at higher deflections, which may be beneficial during low-speed manoeuvers and landing at increased angle of attack by reducing touchdown severity and distance, and consequently, the risk of UAV damage.

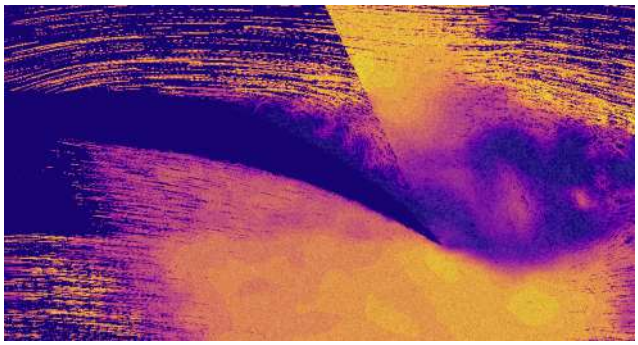
The wind tunnel experiment was conducted on two UAV wing geometries. The UAV equipped with a wing based on the non-cambered NACA 24012 airfoil is referred to as Airfoil 1, while the UAV with the cambered morphing airfoil is referred to as Airfoil 2. Figure 8 presents the lift coefficient, drag coefficient, and pitching moment coefficient characteristics, along with a comparison of these parameters for two airflow velocities: 20 m/s and 25 m/s.



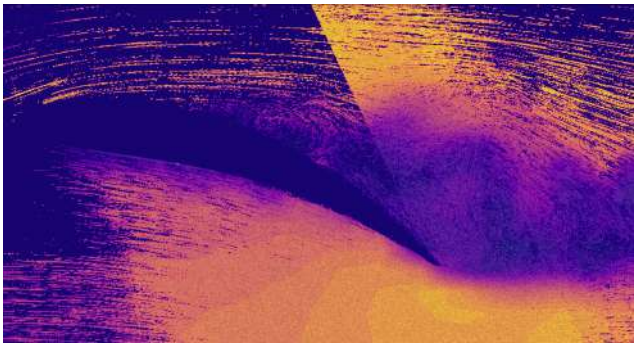
(a) Airfoil 2 $\alpha = 0^\circ$



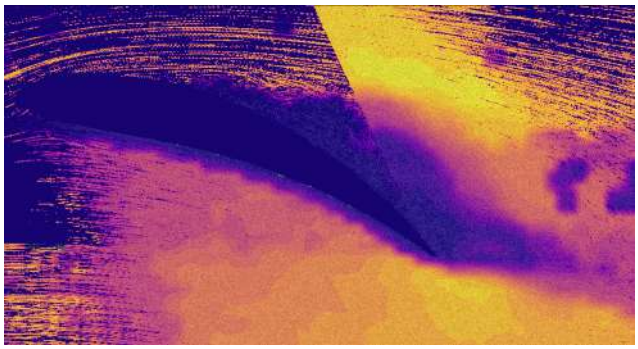
(b) Airfoil 2 $\alpha = 2^\circ$



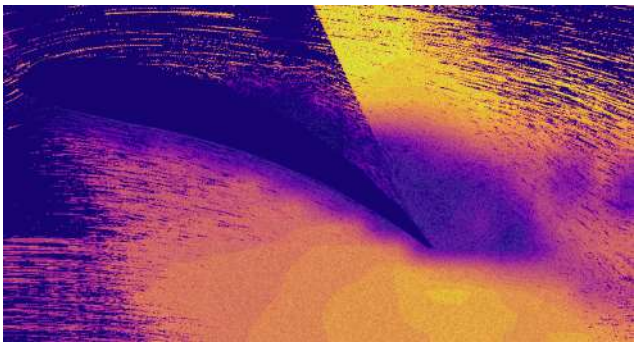
(c) Airfoil 2 $\alpha = 4^\circ$



(d) Airfoil 2 $\alpha = 6^\circ$



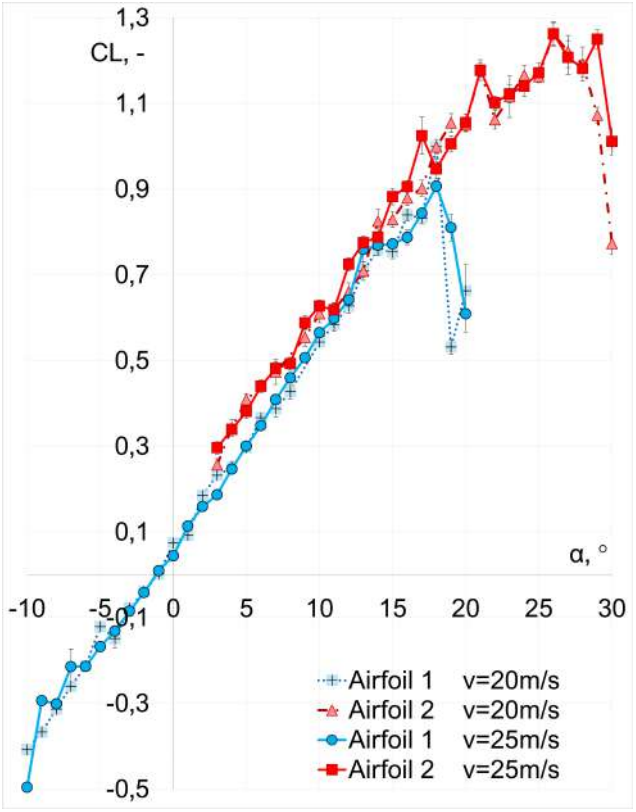
(e) Airfoil 2 $\alpha = 8^\circ$



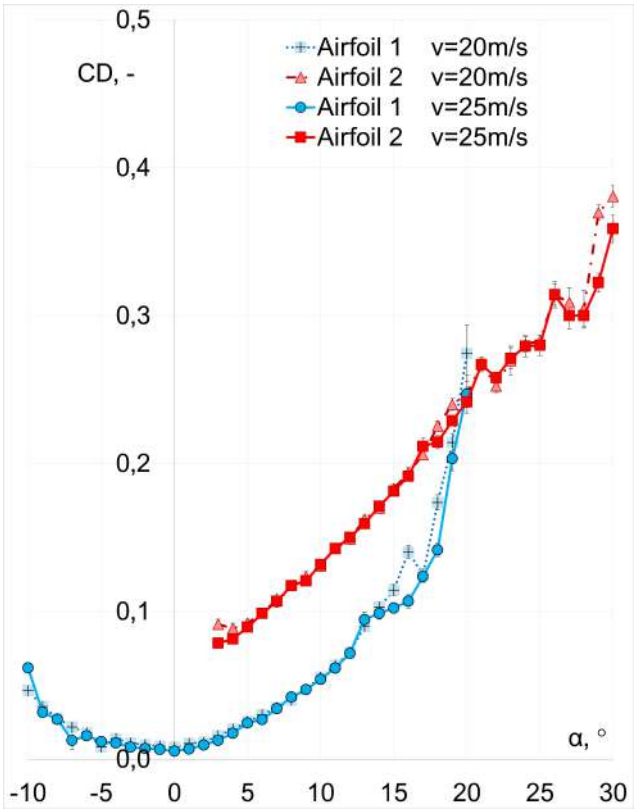
(f) Airfoil 2 $\alpha = 10^\circ$

Figure 7 – PIV results with visible streamlines and velocity field distribution around the Airfoil 2.

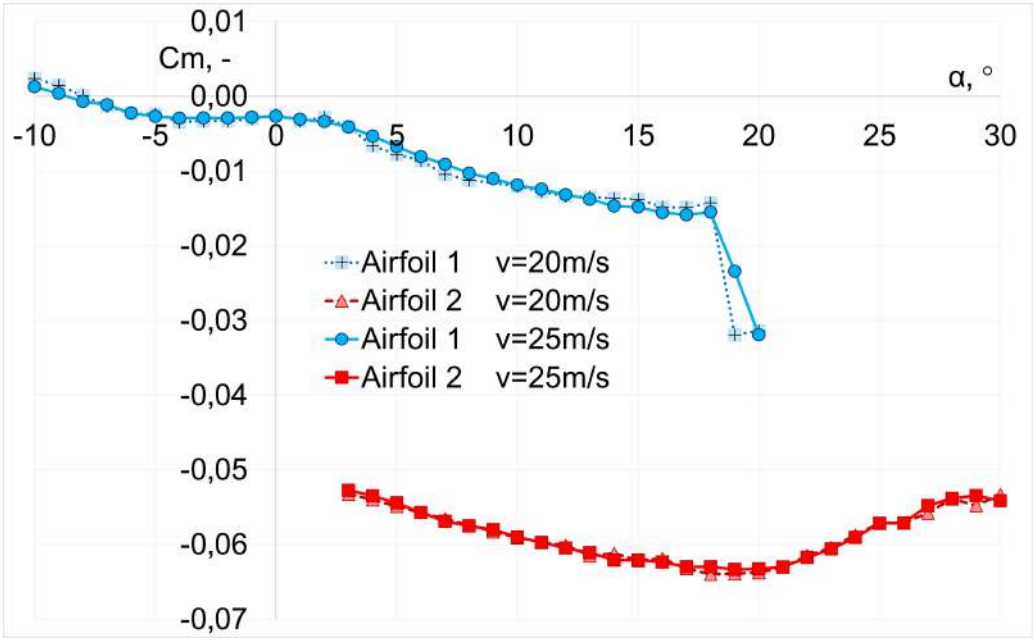
In the Figure 8a, the lift coefficient increases significantly with greater camber deflection. For Airfoil 1 (NACA 24012) at v=20 m/s, the maximum lift coefficient is $C_L = 1.00$ at an $\alpha = 18^\circ$, whereas for the cambered airfoil (Airfoil 2) it reaches $C_L = 1.26$ at $\alpha = 26^\circ$. Thus, increasing the deflection not only raises the maximum lift coefficient but also shifts the critical angle of attack to higher values. Furthermore, at speed 25 m/s, the maximum observed lift coefficient is $C_L = 0.90$ at $\alpha = 18^\circ$ for the non-cambered airfoil, and $C_L = 1.26$ at $\alpha = 26^\circ$ for the cambered one. It can therefore be concluded that the change in flow velocity does not significantly affect the flow behavior or aerodynamic coefficients for the tested geometries. For $\alpha = 10^\circ$ and 20 m/s, the drag coefficient (Figure 8b) increases from $C_D = 0.0555$ for Airfoil 1 to $C_D = 0.1307$ for Airfoil 2. At the higher velocity of 25 m/s, a similar relationship is observed, as for Airfoil 1 $C_D = 0.0541$, while for Airfoil 2 $C_D = 0.1317$. It can be observed that even a minor trailing-edge deflection causes a significant increase in the drag coefficient. The pitching moment coefficient (Figure 8c) decreases for Airfoil 1 across the entire α range at both tested velocities, indicating that the UAV maintains static stability within the useful angle of attack range. However, the Airfoil 2 characteristics show that the cambered airfoil exhibits static stability only up to $\alpha = 20^\circ$. Beyond this angle, the UAV becomes statically unstable.



(a)



(b)



(c)

Figure 8 – Aerodynamic characteristics of tested models: (a) lift coefficient $C_L(\alpha)$, (b) drag coefficient $C_D(\alpha)$, (c) momentum coefficient $C_M(\alpha)$

To sum up, the cambered morphing configuration exhibits a clear increase of the lift coefficient and a shift of the critical angle of attack towards higher values when compared to the baseline configuration, indicating delayed stall and an extended usable range of angles of attack. The change of the velocity does not demonstrate any significant difference in aerodynamic lift force coefficient.
This shows the stability of the presented morphing solution at various velocities. Similarly, a considerable increase in drag is observed even for relatively small trailing-edge deflections, demonstrating that camber morphing may serve as an effective mechanism for controllable drag production. In prin-

ciple the wing deflection is occurring real-time, therefore continuous change of the camber enables significant increases in drag.

4. Summary

The research was conducted to evaluate a continuous trailing-edge morphing wing concept intended to increase the operational flexibility of a micro-UAV operating in hazardous and unprepared terrain. Two complementary experimental setups were employed: Particle Image Velocimetry in a closed-circuit water tunnel to identify flow-field mechanisms, and aerodynamic coefficient measurements in an open-circuit wind tunnel to quantify the integrated performance of two wing configurations. The PIV results have shown that increasing camber deflection changes the flow behavior by promoting the formation of vortical structures above the upper surface and enlarging the aerodynamic wake, which indicates simultaneous lift augmentation and drag growth. The wind tunnel measurements confirm that the morphed configuration provides higher lift, delayed stall, and a pronounced increase in drag compared to the baseline airfoil. Overall, the obtained results indicate that active camber deflection enables increased mission flexibility by supporting speed management, target observation, and decision-making during approach, including the possibility of landing continuation or go-around when operating in hazardous and unprepared landing sites. The continuous morphing of the airfoil allows controllable lift and drag management, which may be advantageously applied to reduce landing distance, mitigate touchdown loads, support mission execution and decision-making in demanding operational environments.

5. Contact Author Email Address

Mailto: marta.marciniuk@pwr.edu.pl

6. Copyright Statement

The authors confirm that they, and/or their company or organization, hold copyright on all of the original material included in this paper. The authors also confirm that they have obtained permission, from the copyright holder of any third party material included in this paper, to publish it as part of their paper. The authors confirm that they give permission, or have obtained permission from the copyright holder of this paper, for the publication and distribution of this paper as part of the ICAS proceedings or as individual off-prints from the proceedings.

References

[1] Terrence A Weisshaar. Morphing aircraft systems: historical perspectives and future challenges. *Journal of aircraft*, 50(2):337–353, 2013.

[2] Tuba Majid and Bruce W Jo. Comparative aerodynamic performance analysis of camber morphing and conventional airfoils. *Applied Sciences*, 11(22):10663, 2021.

[3] Andres E Rivero, Stephane Fournier, Marinos Manolesos, Jonathan E Cooper, and Benjamin KS Woods. Experimental aerodynamic comparison of active camber morphing and trailing-edge flaps. *AIAA Journal*, 59(7):2627–2640, 2021.

[4] D Kumar, S Faruque Ali, and A Arockiarajan. Structural and aerodynamics studies on various wing configurations for morphing. *IFAC-PapersOnLine*, 51(1):498–503, 2018.

[5] Marta Marciniuk, Paweł Piskur, Łukasz Kiszkowiak, Łukasz Malicki, Krzysztof Sibilski, Katarzyna Strzelecka, Stanisław Kachel, and Zygmunt Kitowski. Aerodynamic analysis of variable camber-morphing airfoils with substantial camber deflections. *Energies*, 17(8):1801, 2024.

[6] Sijia Jia, Zhenkai Zhang, Haibo Zhang, Chen Song, and Chao Yang. Wind tunnel tests of 3d-printed variable camber morphing wing. *Aerospace*, 9(11):699, 2022.

[7] Marta Marciniuk, Łukasz Kiszkowiak, Paweł Piskur, Łukasz Malicki, Katarzyna Strzelecka, Krzysztof Sibilski, and Stanisław Kachel. Aerodynamic analysis of camber morphing airfoils using particle image velocimetry and computational fluid dynamics methods. In *34th Congress of the International Council of the Aeronautical Sciences (ICAS 2024)*, 2024.

[8] Monika Prokurat, Katarzyna Elżbieta Grudnik, Stanisław Niemczyk, Wojciech Niemczyk, Karolina Lau, and Janusz Kasperczyk. The use of drones in emergency medicine. *EMERGENCY MEDICAL SERVICE*, 10(2):128–133, 2023.

[9] R Jini Raj, N Praveen, HV Srikanth, and Anil Umesh Bhat Mohammed Nijal. Aerodynamic analysis of bio-inspired wing with adaptive aspect ratio. *Journal of Polymer Composites*, 11(Special Issue 13):143–153, 2023.

[10] CEZARY Galiński and R Żbikowski. Some problems of micro air vehicles development. *Bulletin of the Polish Academy of Sciences Technical Sciences*, pages 91–98, 2007.

[11] Syed Agha Hassnain Mohsan, Nawaf Qasem Hamood Othman, Yanlong Li, Mohammed H Alsharif, and Muhammad Asghar Khan. Unmanned aerial vehicles (uavs): Practical aspects, applications, open challenges, security issues, and future trends. *Intelligent service robotics*, 16(1):109–137, 2023.

[12] Faiyaz Ahmed, Jagannath Chandra Mohanta, Anupam Keshari, and Pankaj Singh Yadav. Recent advances in unmanned aerial vehicles: a review. *Arabian Journal for Science and Engineering*, 47(7):7963–7984, 2022.

[13] Anna Michalska, Daniel Michalski, and Stepan Savchuk. Reliability of unmanned aerial vehicles: winglets' issue. *Aviation and Security Issues*, 3(1):353–367, 2023.

[14] Guillaume Jouvet, Yvo Weidmann, Eef Van Dongen, Martin P Lüthi, Andreas Vieli, and Jonathan C Ryan. High-endurance uav for monitoring calving glaciers: Application to the inglefield bredning and eqip sermia, greenland. *Frontiers in Earth Science*, 7:206, 2019.

[15] Marta Marciniuk, Paweł Piskur, Łukasz Kiszkowiak, Łukasz Malicki, Krzysztof Sibilski, Katarzyna Strzelecka, and Stanisław Kachel. *Badania doświadczalne i numeryczne profili o zmiennej strzałce ugi@ ecia do zastosowań dla bezzałogowych statków powietrznych*, pages 147–163. Mechanika w Lotnictwie ML-XXI 2024, 2024.

[16] Daniel Lichoń, Anna Mikołajczyk, Łukasz Kiszkowiak, and Tomasz Łącki. Identification of uav static aerodynamic characteristics in the water tunnel balance research. *Advances in Mechanical and Materials Engineering*, 33(293 (2)):127–140, 2016.

[17] Krzysztof Sibilski, Mirosław Nowakowski, Dariusz Rykaczewski, Paweł Szczepaniak, Andrzej Żyluk, Anna Sibilska-Mroziewicz, Michał Garbowski, and Wiesław Wróblewski. Identification of fixed-wing micro aerial vehicle aerodynamic derivatives from dynamic water tunnel tests. *Aerospace*, 7(8):116, 2020.

[18] M Kerho and BR Kramer. *Research Water Tunnels—Specification*. Rolling Hills Research Corporation (RHRC): El Segundo, CA, USA, 2003.

[19] William Thielicke and René Sonntag. Particle image velocimetry for matlab: Accuracy and enhanced algorithms in pivlab. *Journal of Open Research Software*, 9(1), 2021.

[20] Paweł Piskur. Side fins performance in biomimetic unmanned underwater vehicle. *Energies*, 15(16):5783, 2022.